Applied Catalysis B: Environmental 181 (2016) 352–362

Contents lists available at ScienceDirect

Applied Catalysis B: Environmental

journal homepage: www.elsevier.com/locate/apcatb

Reduced graphene oxide–CuO nanocomposites for photocatalytic conversion of CO_2 into methanol under visible light irradiation

Rashi Gusain, Pawan Kumar, Om P. Sharma, Suman L. Jain, Om P. Khatri*

Chemical Sciences Division, CSIR—Indian Institute of Petroleum, Dehradun 248005, India

ARTICLE INFO

Article history:
Received 21 May 2015
Received in revised form 31 July 2015
Accepted 5 August 2015
Available online 7 August 2015

Keywords:
Copper oxide nanorods
Reduced graphene oxide
Photocatalysis
CO_2 reduction
Methanol

ABSTRACT

Reduced graphene oxide (rGO)–copper oxide nanocomposites are prepared by covalent grafting of CuO nanorods on the rGO skeleton. Chemical and structural features of rGO–CuO nanocomposites are probed by FTIR, XPS, XRD and HRTEM analyses. Photocatalytic potential of rGO–CuO nanocomposites is explored for reduction of CO_2 into the methanol under the visible light irradiation. The breadth of CuO nanorods and the oxidation state of Cu in the rGO–CuO/Cu_2O nanocomposites are systematically varied to investigate their photocatalytic activities. The pristine CuO nanorods exhibited very low photocatalytic activity owing to fast recombination of charge carriers and yielded 175 $\mu mol\, g^{-1}$ methanol, whereas rGO–Cu_2O and rGO–CuO exhibited significantly improved photocatalytic activities and yielded five (862 $\mu mol\, g^{-1}$) and seven (1228 $\mu mol\, g^{-1}$) folds methanol, respectively. The superior photocatalytic activity of CuO in the rGO–CuO nanocomposites was attributed to slow recombination of charge carriers and efficient transfer of photo-generated electrons through the rGO skeleton. This study further excludes the use of scavenging donor.

1. Introduction

Accumulation of carbon dioxide (CO_2) in the environment is rising at an alarming rate and has become a major cause of the global warming [1]. In the recent past, the use of fossil fuels had increased significantly, which is responsible for higher CO_2 emission and depletion of these resources. The photocatalytic conversion of CO_2 into the fuels like methane, methanol, formic acid etc. based on light irradiation could help at some extent to reduce the CO_2 in the environment and meet the increasing demand of energy [2–4]. During the 80s, Inoue et al. reported for the first time the photocatalytic reduction of CO_2 into valuable chemicals using various semiconductors based catalytic materials [5]. Conversion of CO_2 by photocatalysis, artificial photosynthesis, electrochemical, chemical and biological approaches not only mitigate increasing level of CO_2 in the environment but also provides alternative fuel and valuable chemicals [6–8]. Till date, several photocatalysts such as TiO_2, inorganic metal complexes, metal oxide, metal sulphides, carbon-based composites etc. along with co-catalyst/photo sensitizers have been demonstrated for the photoreduction of CO_2 under the light irradiation [9–21]. Band gap energy of semiconductors plays an important role to control the photocatalytic activity of nanomaterials and it should be in an appropriate range to absorb the visible light [22]. Most of metal oxide semiconductors are unable to absorb visible light because of their wide band gap. While, small band gap containing semiconductors exhibit fast recombination phenomenon, hence photo-generated holes and electrons unable to act efficiently for photocatalytic conversion. The recombination time can be delayed by monitoring the defect density in the semiconductor lattice, trapping the photo-generated electrons or holes by introduction of co-catalyst, doping of hetero-atom and functionalization of photocatalysts [23–25]. The organic reducing agents *e.g.*, triethanolamine, triethylamine, alcohols etc. have been used as hole scavengers to oxidize holes; simultaneously, freely available photo-electrons can reduce the CO_2 into the chemicals [26,27]. Water and other protic solvents have also been used for photocatalytic hydrogenation of CO_2. The nanostructural semiconductor based catalysts provide active sites for adsorption of CO_2 where the photo-generated electrons could reduce CO_2 into the desired products [28]. The presence of co-catalyst/photo sensitizers further facilitates the photocatalytic activity and enhanced the conversion rate.

Graphene, a most emergent material of current decade, promises immense potential for large range of applications including transistors, optoelectronics, polymer composite, drug delivery, hydrogen production, energy storage devices, sensors, lubrication, catalysis to name a few [29–34]. Recently, graphene-based materials have been gaining large interest as promising candidate

* Corresponding author. Fax: +91 135 2660200.
E-mail addresses: opkhatri@iip.res.in, khatriopk@gmail.com (O.P. Khatri).

http://dx.doi.org/10.1016/j.apcatb.2015.08.012
0926-3373/

for photocatalytic activities owing to their unique characteristics such as high specific surface area, high adsorption capacity, excellent mobility of electrons, ease of chemical modification and electrochemical stability [35]. The graphene oxide (GO) as a semiconductor photocatalyst with an apparent band gap of 2.4–4.3 eV, generates hydrogen by splitting of water under light irradiation, however, during the photocatalytic process, GO losses oxygen functionalities and bandgap gradually reduced toward the rage of conductive materials [36]. The reduced graphene oxide (rGO) grafted with semiconductor material has the unique ability to store and shuttle electrons *via* electron transfer process, which is very crucial for photocatalytic reactions [37]. The TiO_2–rGO nanocomposite as a photocatalyst exhibits great adsorptivity of dyes, extended light absorption range and efficient charge separation properties, which eventually leads to efficient photo-degradation of organic dyes [38].

Low-cost copper-based semiconductors, which are abundantly available in the earth crust, are gaining large interest for photocatalytic reactions. The nanocomposites of Cu, Cu_2O and CuO with TiO_2 demonstrated excellent photocatalytic activities compared to bare and the noble metal loaded TiO_2 [38–40]. The bare copper oxide absorbs visible light efficiently, however, fast recombination events hold back its potential for the photocatalytic activities [41]. Recently Tian et al. demonstrated that CuO/Cu_2O/Cu nanorods-decorated rGO composite generates photo-current under visible light irradiation, where the rGO not only accepts the electrons from the CuO–Cu_2O–Cu nanorods but also facilitates electrons transfer within the composite [42]. Herein, we have prepared nanocomposites based on rGO and copper oxide (CuO and Cu_2O) nanomaterials. These nanocomposites were evaluated for their potential to photocatalytic conversion of CO_2 into the methanol under the visible light irradiation. The breadth of CuO nanorods grafted on the rGO skeleton found to control the photocatalytic efficiency. Chemical and structural features of nanocomposites were thoroughly characterized by FTIR, XRD, XPS and HRTEM.

2. Experimental

2.1. Materials

Graphite powder (Sigma–Aldrich), sodium nitrate (98%, Alfa Aesar), $KMnO_4$ (99%, Fischer Scientific), H_2SO_4, copper(II) acetate monohydrate (98%, SDFCL), NaOH pellets (98%, Fischer Scientific), 3-aminopropyltrimethoxysilane (APTMS; 97%, Sigma–Aldrich) were used without further purification.

2.2. Synthesis of rGO–CuO nanocomposites

Initially the CuO nanorods and the GO, precursors to rGO–CuO/Cu_2O nanocomposites, were synthesized individually. In a typical procedure, CuO nanorods were prepared by simple mixing of $Cu(CH_3COO)_2{\cdot}H_2O$ with aqueous solution of NaOH at room temperature for two hours under uninterrupted stirring. In order to prepare, different sizes of CuO nanorods, 0.0125 mol of $Cu(CH_3COO)_2{\cdot}H_2O$ was mixed with different molar concentrations of NaOH (0.05, 0.1, 0.2 and 0.3 mol). The synthesized CuO nanorods were collected by centrifugation at 3000 rpm and then were washed several times with water to remove the physisorbed reaction precursors. Ethanol was used for the final washing. The CuO nanorods prepared by using 0.05, 0.1, 0.2 and 0.3 moles of NaOH were named as CuO14, CuO18, CuO116 and CuO124, respectively. A 950 mg of CuO was yielded in the each reaction batch. The GO was synthesized by harsh oxidation of graphite powder using $NaNO_3$, H_2SO_4 and $KMnO_4$ as strong oxidizing reagents and then ultrasound-assisted exfoliation of the oxidized product [43]. The GO was then reduced into the rGO using hydrazine hydrate as a reducing agent (Scheme 1c and d) to restore the graphitic characteristics. This was followed by introduction of selective oxygen functionalities at the edge and defect sites of 50 mg rGO *via* mild oxidation using the nitric acid as an oxidizing reagent (Scheme 1d and e) [44]. In a parallel step, wet cake of CuO nanorods was thoroughly dispersed in the toluene and then purged with nitrogen. A 1.5 mL APTMS was added to the CuO dispersion and the resulting mixture was refluxed overnight with continuous stirring under the nitrogen atmosphere. At completion of the reaction, the mixture was allowed to cool down and then centrifuged at 3000 rpm for 10 min. The APTMS-functionalized CuO nanorods (Scheme 1b) were washed several times with toluene and then rinsed with ethanol and water in the subsequent order. The APTMS-functionalized CuO nanorods having amino functionality as a head group, was thoroughly mixed with aqueous dispersion of selectively oxidized rGO nanosheets and the pH of the reaction mixture was maintained as ~10. The temperature of alkaline reaction mixture was raised to 80 °C and reaction was carried out for 15 h under uninterrupted stirring. The synthesized rGO–CuO nanocomposite (Scheme 1f) having 1:20 ratio of rGO and CuO was washed several times with water and ethanol, and then dried at 65 °C for 6 h in the air-oven. The synthesized nanocomposites of rGO with CuO14, CuO18, CuO116 and CuO124 nanorods, were coined as rGO–CuO14, rGO–CuO18, rGO–CuO116 and rGO–CuO124, respectively. For a comparison purpose, rGO–Cu_2O116 nanocomposite was prepared by hydrothermal reduction of rGO–CuO116. In this context, a Parr reactor bomb was charged with aqueous dispersion of rGO–CuO116 nanocomposite. The hydrothermal reduction was carried out at 300 °C for 2 h. At completion of the reaction, reactor bomb was allowed to cool down under ambient condition. The developed product (rGO–Cu_2O116) was washed with water and ethanol in subsequent order, and then dried at 65 °C in the air- oven.

2.3. Chemical and structural characterizations

The crystalline nature of rGO–CuO/Cu_2O nanocomposites was examined by powder X-ray diffraction (XRD) using a Bruker D8 Advance diffractometer operated with Cu Kα radiation of 0.15418 nm wavelength at 40 kV and 40 mA. The chemical features of all nanocomposites were probed by Fourier transform infrared (FTIR) and X-ray photoelectron spectroscopy (XPS). FTIR measurements were carried out using a Thermo-nicolet 8700 Research spectrometer with a resolution of 4 cm^{-1}. XPS analyses were carried out using a JPS-9010TRX electron spectrophotometer. High-resolution transmission electron microscopy (HRTEM) of rGO–CuO/Cu_2O nanocomposites was carried out to probe the nanostructural features and their lattice fringes. UV–vis absorbance spectra of all samples were taken by using a Shimadzu UV-2600 spectrophotometer. The $BaSO_4$ was used as reference material for UV–vis measurements. The Brunauer–Emmett–Teller (BET) surface area, pore volume and average pore size of all samples were obtained from the N_2 adsorption/desorption isotherms using BELSORP max (Japan) surface area analyzer at 77 K. The samples were degassed and dried under a vacuum at 250 °C for 4 h prior to measurement.

2.4. Photocatalytic reactions

The photocatalytic experiments for CO_2 reduction were carried out using rGO–CuO14, rGO–CuO18, rGO–CuO116, rGO–CuO124, rGO–Cu_2O116, CuO116 and rGO as the photocatalysts. In a typical experiment, a 100 mL cylindrical vessel (ϕ = 5 cm) made of borosilicate glass, was charged with a mixture of DMF (45 mL) and water (5 mL). It was purged with nitrogen gas for 15 min to degas the reaction mixture. This was followed by purging of the solution

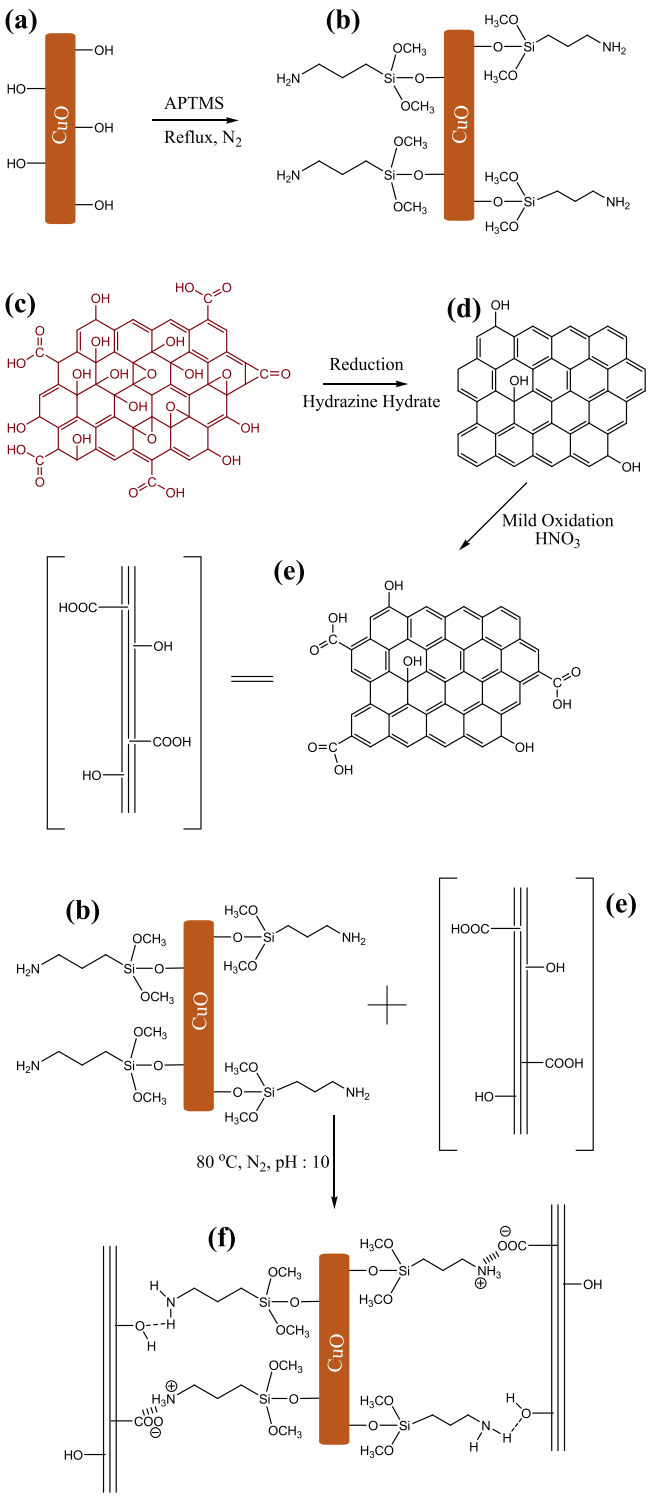

Scheme 1. Schematic model of (a) CuO and (b) APTMS-functionalized CuO nanorods. APTMS was grafted on the CuO nanorods by chemical interaction between methoxy groups of APTMS and hydroxyl functionalities decorated on the CuO nanorods. (c) GO, (d) rGO and (e) selectively oxidized rGO nanosheets. The rGO was prepared by reduction of GO using hydrazine hydrate as a reducing agent. The defect and edge sites of rGO were then converted into carboxylic and hydroxyl groups *via* its mild oxidation with HNO3. (f) In the subsequent step, CuO nanorods were grafted on the GO skeleton *via* charge induced and hydrogen interaction between the amino group of APTMS-functionalized CuO nanorods and carboxylic and hydroxyl functionalities of rGO, respectively.

with CO_2 gas for 30 min under continuous stirring to saturate the solution with CO_2. The 100 mg photocatalyst was added to reaction mixture and vessel was sealed with a septum. Reaction vessel was irradiated to visible light using a 20 W white cold LED flood light. The distance between the reaction vessel and light source was maintained as 5 cm and irradiated intensity on reaction vessel was found to be 85 W m^{-2}. The reaction progress was monitored by collecting and then analyzing the sample at regular interval. The each sample was analyzed by injecting in GC-FID (Varian CP3800 by using CP Sil 24CB LOW BLEED/MS column, flow rate: 0.5 mL min^{-1}, injector temperature: 250 °C, FID detector temperature: 275 °C) for quantitative determination. In order to check the linear response of GC-FID over different concentration and quantification of product, a calibration curve was prepared using standard samples of methanol. Furthermore, photocatalytic reaction product was characterized by HPLC (Shimadzu UFLC, by using Oyster BDS Premium C18 250 × 4.6 mm, 5 μm column mobile phase acetonitrile:acetone 60:40, flow rate 0.5 mL min^{-1} at wavelength of 205 nm). Gaseous products were determined with the help of GC-TCD and GC-FID (Agilent 7890A GC system) using capillary column (RGA, refinery gas analyzer) at the flow rate of 35 mL min^{-1} for H_2, 350 mL min^{-1} for air, 27 mL min^{-1} for makeup flow, 45 mL min^{-1} for TCD reference flow and 2 mL min^{-1} for helium flow; injector temperature: 220 °C, TCD detector and FID detector temperature: 220 °C. For determining the gaseous products 20 μL sample was injected in GC and then yield was correlated by injecting standard gaseous mixture. Blank reactions were carried out to ensure that originated methanol was photoreduction product of CO_2. In the first blank reaction, no catalyst was added and all other conditions were maintained the same; while in the second reaction, same catalyst and solvent system were used except reaction was conducted in the dark. A third additional blank experiment was conducted by visible-illuminating reaction vessel having the catalyst, but was purged with N_2 rather than CO_2.

3. Results and discussion

The CuO nanorods were synthesized by facile chemical processing of aqueous solution of copper acetate monohydrate and variable molar ratio of sodium hydroxide at the room temperature. The APTMS was used as a bi-functional linker to graft the CuO nanorods on the rGO skeleton *via* chemical interaction as demonstrated in Scheme 1. The crystal structure and composition of rGO–CuO nanocomposites were examined by powder XRD measurements. XRD patterns of rGO–CuO nanocomposites as shown in Fig. 1 are in good agreement with the JCPDS (05-0661) data of CuO [45]. The major peaks at $2\theta = 35.75°$ and 38.88° were attributed to (1 1 1)/(0 0 2) and (1 1 1)/(2 0 0) planes respectively, and revealed the monoclinic crystallinity of CuO in rGO–CuO nanocomposites. The rGO exhibited very broad diffraction at $2\theta = \sim 24°$ and is corresponding to very few lamellae within the rGO nanosheets along with their corrugated structure (Fig. S1, ESI). The XRD features owing to the rGO could not be appeared in XRD patterns of rGO–CuO nanocomposites because of the strong diffraction pattern of CuO and low concentration of rGO nanosheets [46]. The preparation of rGO–Cu_2O116 by hydrothermal reduction of rGO–CuO116 was confirmed by its XRD pattern (Fig. 1f) and is in complete agreement with the JCPDS date card no. 01-78-2076 of Cu_2O phase [45].

Chemical features and grafting of CuO nanorods on the rGO skeleton were examined by FTIR and XPS measurements. FTIR spectra of rGO–CuO nanocomposites as shown in Fig. 2a exhibit characteristic vibrations at ~2925 and ~2850 cm^{-1}, attributed to methylene asymmetric and symmetric stretches, revealing the presence of APTMS in rGO–CuO nanocomposites. The higher intensities of these vibrations for rGO–CuO14 were attributed to higher

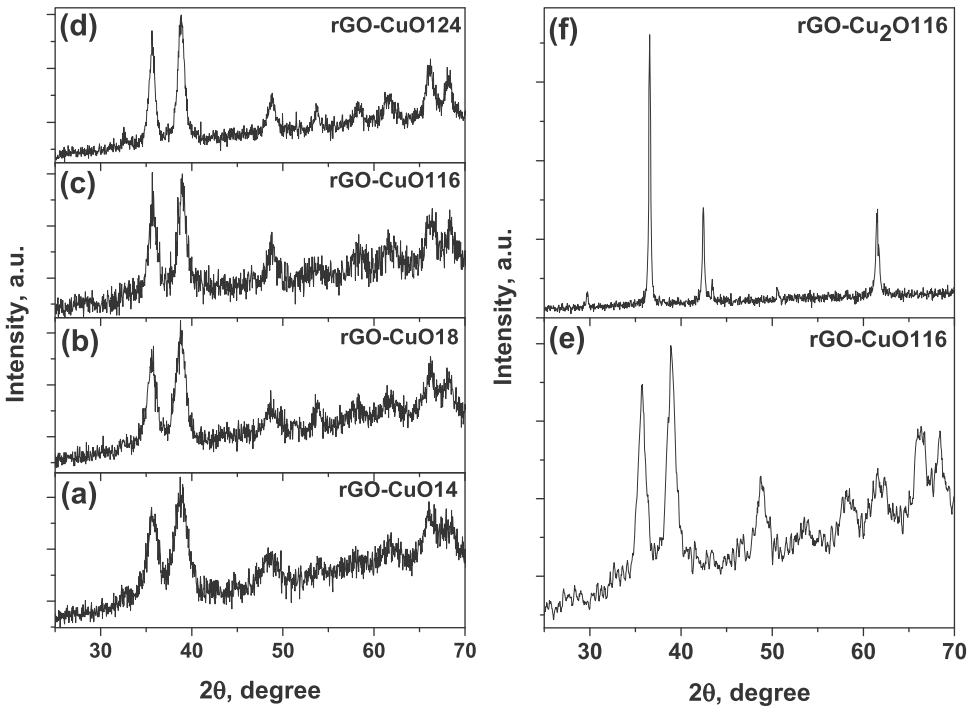

Fig. 1. Powder XRD patterns of (a) rGO–CuO14, (b) rGO–CuO18, (c) rGO–CuO116 and (d) rGO–CuO124 nanocomposites. XRD patterns of (e) rGO–CuO116 and (f) rGO–Cu_2O116 nanocomposites.

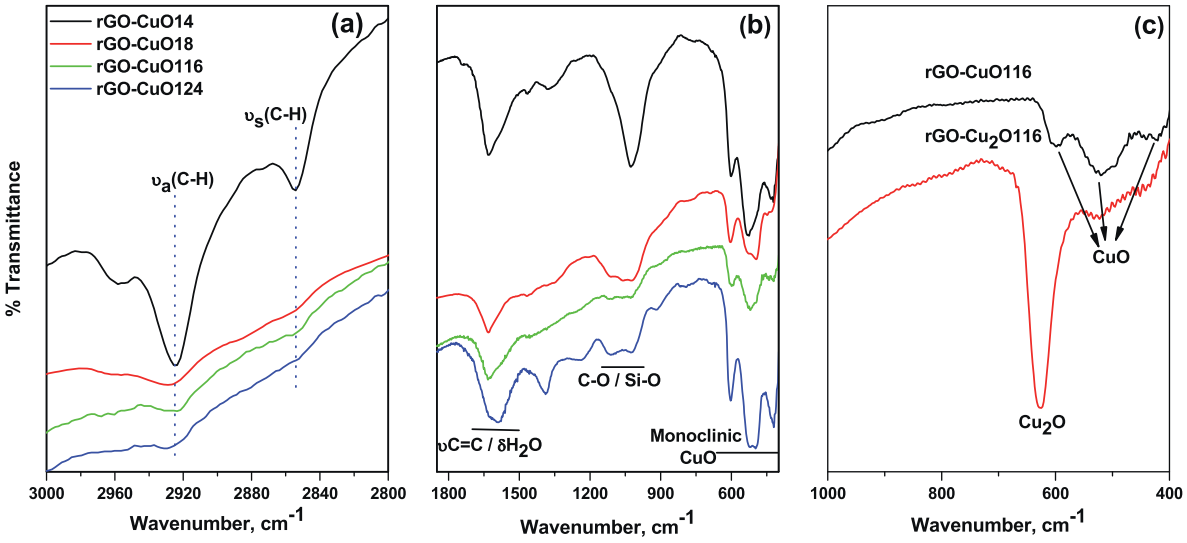

Fig. 2. FTIR spectra of (a and b) rGO–CuO14, rGO–CuO18, rGO–CuO116 and rGO–CuO124 nanocomposites in the spectral range of 3000–2800 and 1850–400 cm^{-1}, respectively. (c) FTIR spectra of rGO–CuO116 and rGO–Cu_2O116 nanocomposites in the spectral range of 1000–400 cm^{-1}, demonstrating IR modes of CuO and Cu_2O.

grafting of APTMS on the CuO14 nanorods owing to their small size and higher specific surface area. Three strong vibrational bands in the range of 600–400 cm^{-1} (Fig. 2b) revealed the monoclinic crystalline structure of CuO in all rGO–CuO nanocomposites. However, rGO–Cu_2O116 (Fig. 2c) exhibits an intense vibrational peak at 625 cm^{-1} which was attributed to the Cu_2O crystalline structure in rGO–Cu_2O116 [47]. The vibrational signatures in the range of 1100–1000 cm^{-1} were associated to the Si—O and C—O linkage in the rGO–CuO nanocomposites. The detailed peak characterizations of all vibrational spectra are depicted in Table S1 (ESI).

Chemical state of constituent elements in the rGO–CuO nanocomposites was probed by XPS measurements. Fig. 3a shows the high-resolution Cu 2p XPS spectra of rGO–CuO nanocomposites. The Cu 2p peaks were seen at ~933.5 eV along with shake-up satellite peaks at higher binding energy, revealing d^9 electronic state of copper and is characteristic to Cu^{2+} oxidation state in all the rGO–CuO nanocomposites [48]. The grafting of CuO116 nanorods on rGO *via* APTMS linker was further confirmed by the appearance of C 1s, N 1s and Si 2p peaks (Fig. 3b–d). High-resolution C 1s spectrum of rGO–CuO116 showed an asymmetric peak structure with a broad shoulder at higher binding energy, attributed to different types of carbon structure. The peak fitting of the C 1s spectrum of rGO–CuO116 could be deconvoluted into chemically shifted three major peak components (Fig. 3b) at 284.5, 287 and 288.4 eV. Among them, a major component at 284.5 eV was contributed by C—C/C—H carbons of rGO skeleton and methylene units of APTMS in the

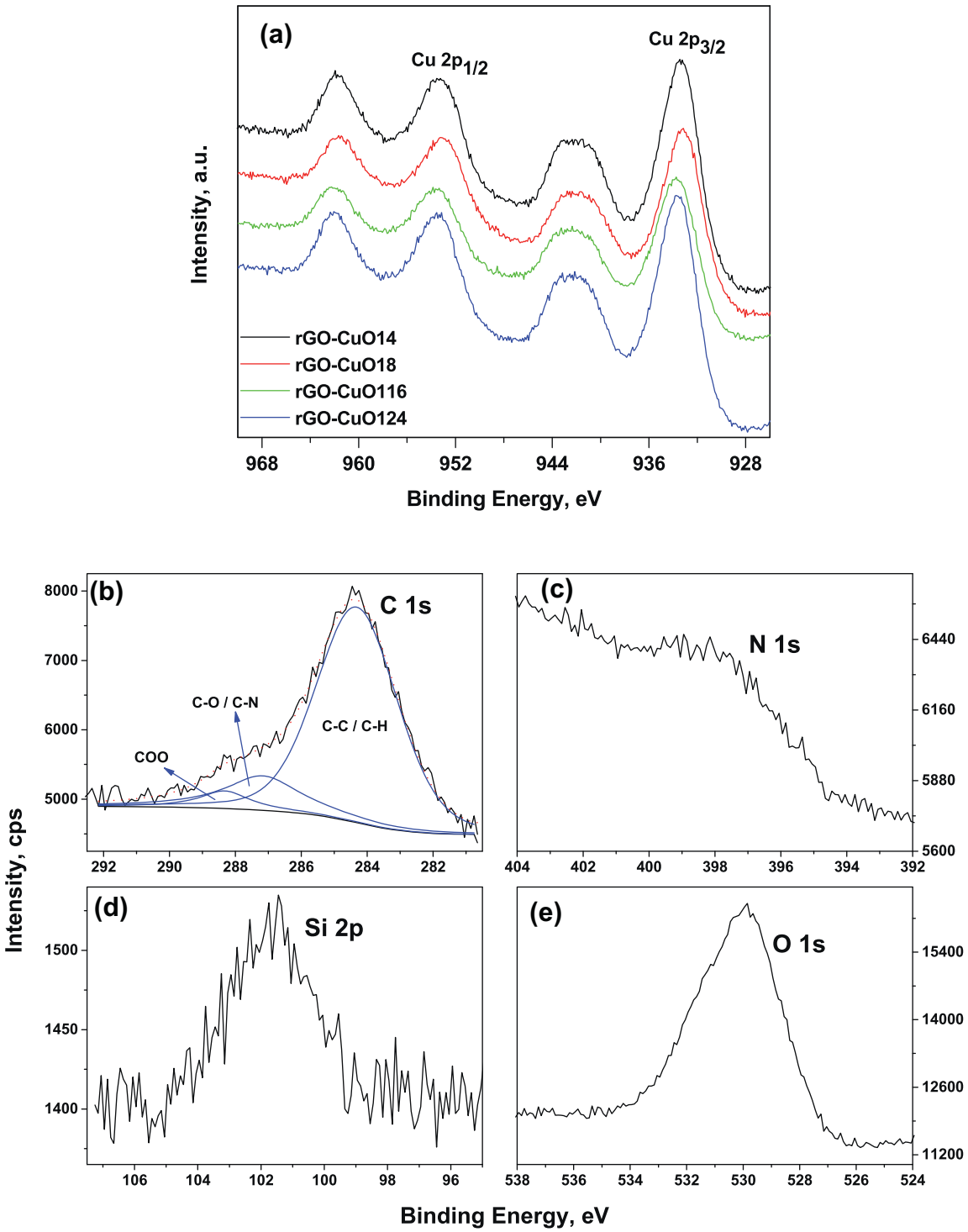

Fig. 3. High resolution (a) Cu 2p XPS patterns of rGO–CuO14, rGO–CuO18, rGO–CuO116 and rGO–CuO124 nanocomposites. High resolution (b) C 1s, (c) N 1s, (d) Si 2p and (e) O 1s XPS peaks of rGO–CuO116 nanocomposites. The deconvoluted peak components in the C 1s spectrum illustrate chemical linkages with various types of functionalities in the rGO–CuO116 nanocomposite.

rGO–CuO116 nanocomposite. A peak component at 287 eV was originated from the residual oxygen functionalities of rGO and C—O linkage between the APTMS and CuO nanorods in the rGO–CuO116 composite. High energy peak component with low intensity at 288.4 eV was due to the environmental contamination to the sample. Importantly, the appearance of N 1s and Si 2p peaks in the rGO–CuO116 nanocomposites further showed that CuO nanorods are grafted on the rGO skeleton *via* APTMS bifunctional thin film. In this context, methoxy groups of APTMS covalently interacted with hydroxyl groups of the CuO nanorods and provided the Si—O linkages, which was confirmed by appearance of Si 2p peak at ~102 eV. The broad peak of N 1s spectrum revealed that amino groups of APTMS-functionalized CuO nanorods plausibly interact with oxygen functionalities of rGO *via* charge–induced interaction, hydrogen bond linkage and covalent interactions [49,50].

The morphological features of rGO–CuO nanocomposites were examined by the HRTEM analysis. The CuO nanorods are randomly distributed on the rGO skeleton in the rGO–CuO nanocomposites as

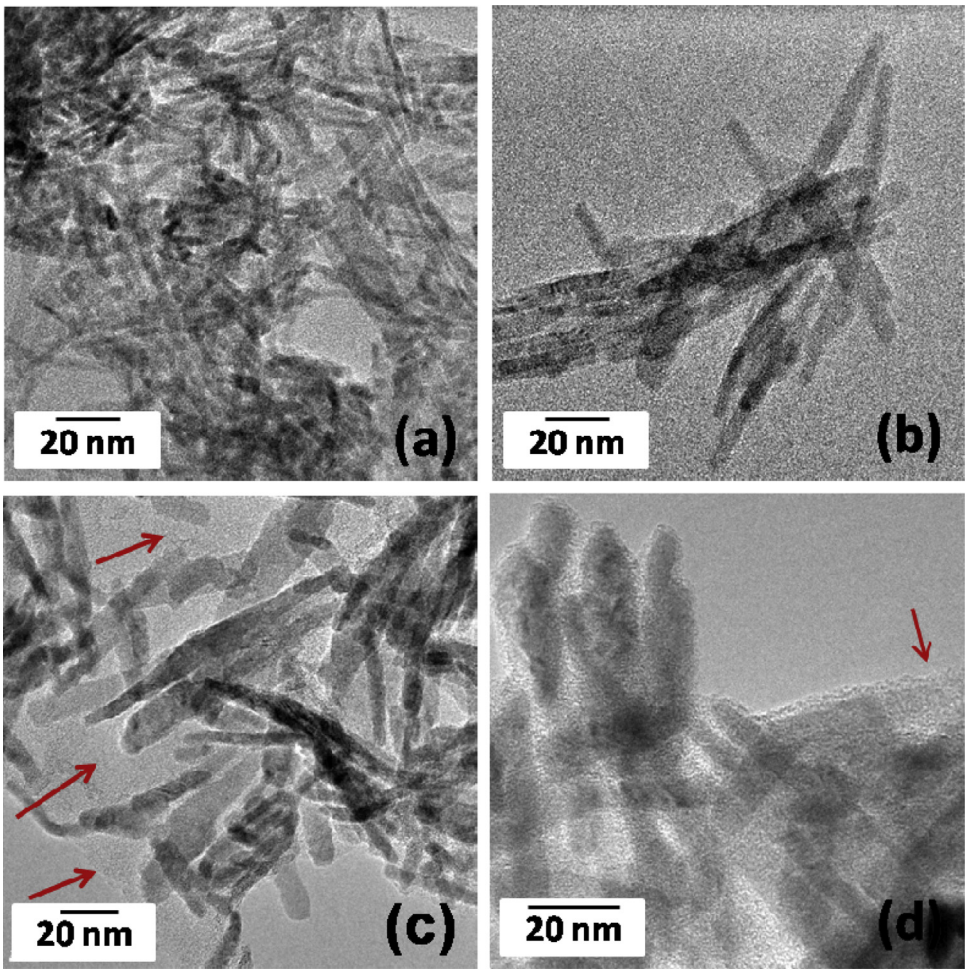

Fig. 4. HRTEM images of (a) rGO–CuO14, (b) rGO–CuO18, (c) rGO–CuO116 and (d) rGO–CuO124 nanocomposites. The rGO nanosheets are shown by red arrows. (For interpretation of the references to color in this figure legend, the reader is referred to the web version of this article.)

shown in Fig. 4. The rGO nanosheets are highlighted by red arrows. An increasing molar ratio of copper salt to NaOH, from 1:4 to 1:24, increases the breadth of CuO nanorods and was found to be 3–6, 5–9, 9–11 and 10–15 nm in rGO–CuO14, rGO–CuO18, rGO–CuO116 and rGO–CuO124 nanocomposites, respectively. For comparison study, rGO–Cu_2O116 was prepared by hydrothermal reduction of rGO–CuO116 nanocomposite. Fig. 5 shows that CuO116 nanorods in rGO–CuO116 were reconfigured to the Cu_2O116 nanoparticles of 3–6 nm diameter. These nanoparticles were thoroughly distributed on rGO skeletone as illustrated in Fig. 5d and e. Furthermore, high resolution images explicitly differenciate the rGO skeleton from the CuO116 nanorods in the rGO–CuO116 (Fig. 5c) and Cu_2O116 nanoparticles in the rGO–Cu_2O116 (Fig. 5e and f). The textural properties of rGO–CuO and rGO–Cu_2O nanocomposites were obtained from their nitrogen adsorption–desorption isotherms (Fig. 6). The higher absorption capacity of rGO–CuO116 could be attributed to the larger surface area and pore volume of the material (Table 1). The pore size distribution of rGO–CuO and rGO–Cu_2O nanocomposites, suggested the presence of mesopores in the materials. The BJH pore size distribution (Fig. 7) revealed that the most of pores in the rGO–CuO14 are below the 10 nm. Both the pore size and the pore size distribution range were further increased with increasing the breadth of CuO nanordos as deduced from Fig. 7. The rGO–CuO18 exhibited largest surface area, *i.e.*, 128.9 $m^2\ g^{-1}$, while rGO–CuO116 showed highest pore volume (0.788 $cm^3\ g^{-1}$) among all the samples being studies for the photocatalytical activities.

Table 1
Textural properties of rGO–CuO14, rGO–CuO18, rGO–CuO116, rGO–CuO124 and rGO–Cu_2O116 nanocomposites.

Sr. no.	Sample description	Pore volume ($cm^3\ g^{-1}$)	BET surface area ($m^2\ g^{-1}$)
1	rGO–CuO14	0.241	87.6
2	rGO–CuO18	0.707	128.9
3	rGO–CuO116	0.788	116.6
4	rGO–CuO124	0.453	95.87
5	rGO–Cu_2O116	0.434	64.06

The influence of the CuO nanorod breadth on optical absorption properties of rGO–CuO nanocomposites were probed by UV–vis absorption spectroscopy. The rGO–CuO nanocomposites shows (Fig. S4, ESI) a wide-range absorption between 200 and 700 nm, attributed to the characteristic absorption of CuO nanoparticles [51]. The characteristic absorption of rGO was overlapped with CuO absorption in the range of 250–270 nm. Interestingly, absorption maxima of rGO–CuO was gradually shifted toward higher wavelength with increasing the breadth of CuO nanorods and found to be maximum for rGO–CuO116. Further, the rGO–CuO116 nanocomposites exhibited maximum absorption ability among all samples being studied.

Photocatalytic potential of rGO–CuO nanocomposites was examined by reduction of CO_2 into methanol by using water/DMF mixture under visible light irradiation. In order to probe the reaction progress, 1 μL liquid sample was withdrawn during the

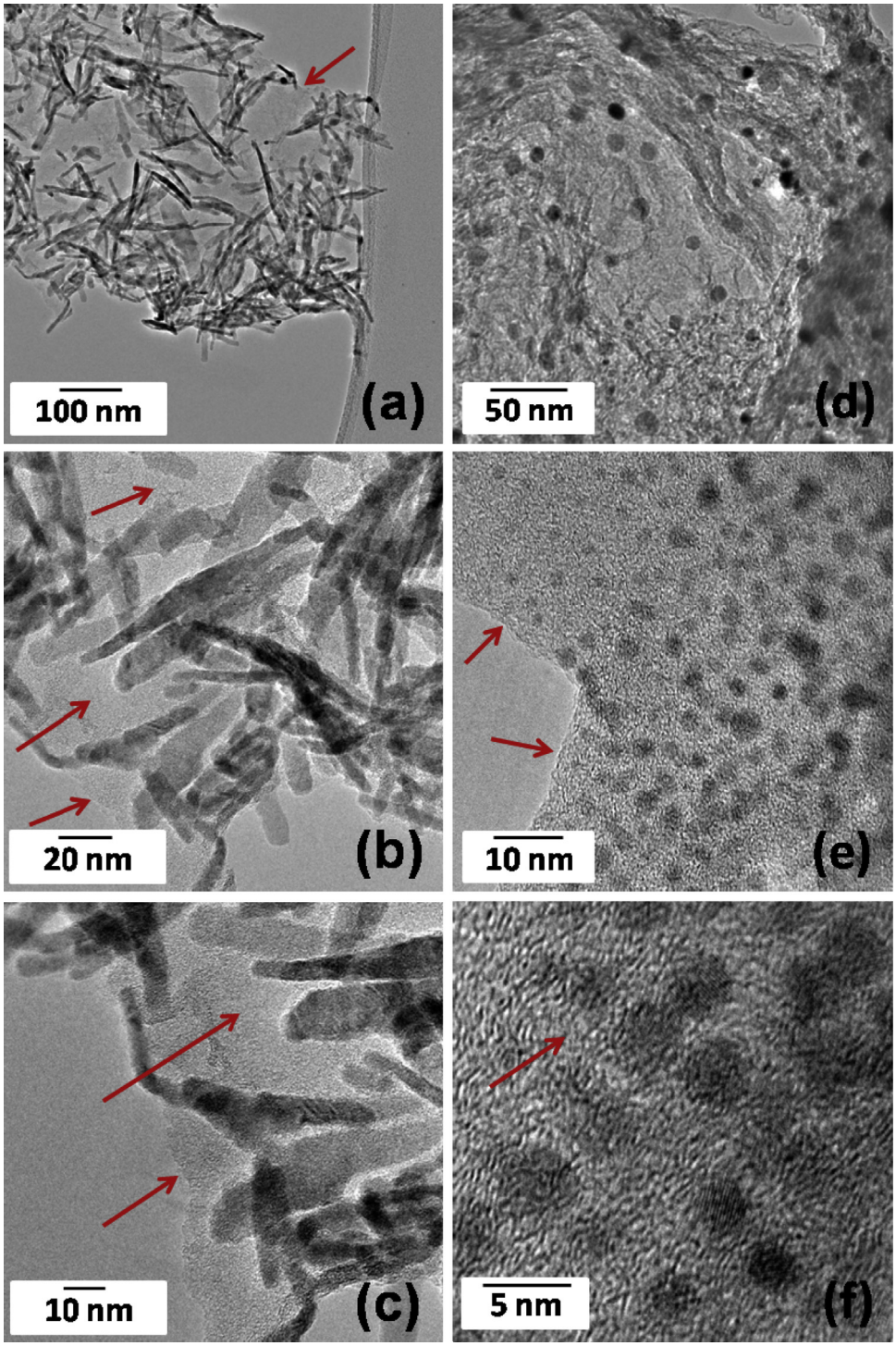

Fig. 5. HRTEM images of (a–c) rGO–CuO116 and (d–f) rGO–Cu_2O116 nanocomposites. During hydrothermal reduction, CuO116 nanorods in rGO–CuO116 are converted into Cu_2O116 nanoparticles (ϕ = 3–6 nm), which are thoroughly distributed on the rGO skeleton. The rGO nanosheets are shown by brown arrows and are explicitly seen in the high resolution images. (For interpretation of the references to color in this figure legend, the reader is referred to the web version of this article.)

photoreduction and analyzed by using a GC/FID system. The results showed the formation of methanol is the only liquid product. The absence of other possible products such as HCOOH and HCHO was confirmed by injecting the standard solutions of respective compounds (Fig. S7). Further confirmation of the absence of other products was done by HPLC (Fig. S8). Hence, the performance of each catalyst was evaluated in terms of methanol yield. The methanol yield (μmol g^{-1} cat) by photocatalytic conversion of CO_2 in water/DMF mixture using rGO–CuO14, rGO–CuO18, rGO–CuO116 and rGO–CuO124 as photocatalysts with light irradiation time is shown in Fig. 8. No methanol was observed in the absence of photocatalyst, whereas rGO–CuO nanocomposites exhibited photocatalytic activity and provided methanol selectively as the photoreduction product of CO_2. The yield of methanol was found to increase with increasing the breadth of CuO nanorods in the rGO–CuO nanocomposites. After 24 h of visible light irradiation, the yield of methanol was found to be 824, 997, 1228 and 1282 μmol g^{-1} cat using rGO–CuO14, rGO–CuO18, rGO–CuO116

Table 2
Photocatalytic reduction of CO_2 into methanol under controlled experimental conditions.[a]

Entry	Catalyst	Reaction precursor	Cat./mg	Visible light illumination	T/h	Methanol yield (μmol g^{-1} cat)
1	None	CO_2	None	Yes	24	None
2	rGO–CuO14	CO_2	100	Yes	24	824
3	rGO–CuO18	CO_2	100	Yes	24	997
4	rGO–CuO116	CO_2	100	Yes	24	1228
5	rGO–CuO116	N_2	100	Yes	24	None
6	rGO–CuO116	CO_2	100	No	24	None
7	rGO–CuO124	CO_2	100	Yes	24	1282
8	rGO–Cu_2O116	CO_2	100	Yes	24	863
9	CuO116	CO_2	100	Yes	24	175
10	rGO	CO_2	100	Yes	24	82

[a] Conditions: solvent system—DMF/water (45/5 mL), visible light source: 20 W LED.

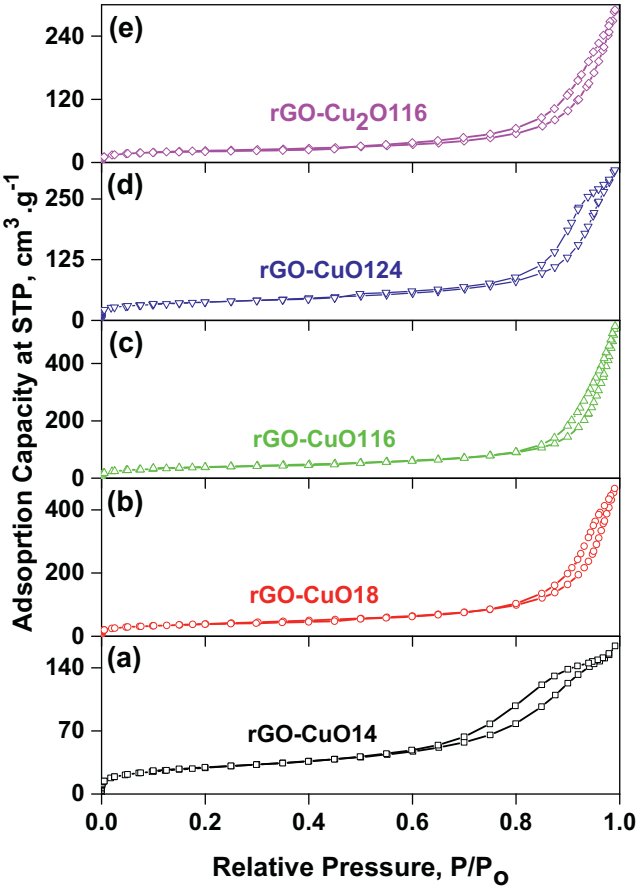

Fig. 6. Nitrogen adsorption–desorption isotherms of (a) rGO–CuO14, (b) rGO–CuO18, (c) rGO–CuO116, (d) rGO–CuO124 and (e) rGO–Cu_2O116 nanocomposites.

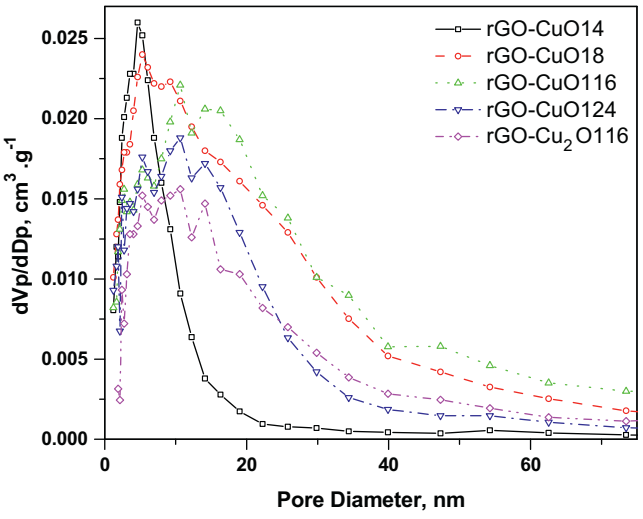

Fig. 7. The BJH pore size distribution rGO–CuO14, rGO–CuO18, rGO–CuO116, rGO–CuO124 and rGO–Cu_2O116 nanocomposites.

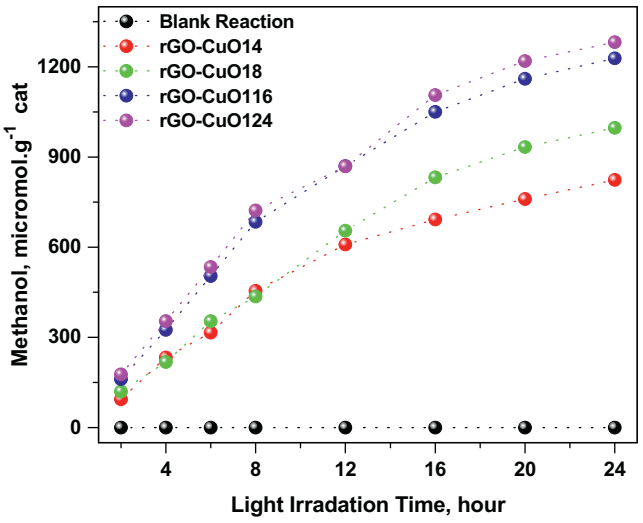

Fig. 8. Methanol yield by photocatalysis of CO_2 as a function of visible light irradiation time using rGO–CuO nanocomposite as photocatalysts.

and rGO–CuO124 photocatalysts, respectively. The formation of methanol was further confirmed by HPLC analysis as shown in Fig. S8. Three blank experiments were further conducted to confirm that methanol was generated because of CO_2 photoreduction. In the absence of photocatalyst (Table 2, entry 1), in the dark conditions (Table 2, entry 6), and using N_2 instead of CO_2 (Table 2, entry 5) showed that no methanol was formed even after 24 h of reaction time. The quantum yield for methanol (ϕ_{MeOH}) was estimated to be 0.008, 0.010, 0.012 and 0.013 in the presence of rGO–CuO14, rGO–CuO18, rGO–CuO116 and rGO–CuO124 nanocomposites, respectively.

Quantum yield of Product ($\phi_{Product}$) = [number of moles of product × number of electrons required for reduction]/[moles of incident photons]

The gaseous products were analyzed by GC-FID and GC-TCD equipped with a RGA column. Gaseous phase analysis showed the presence of hydrogen and oxygen without any evidence for the formation of other gaseous products like CO, CH_4. The yield of hydrogen by using rGO–CuO14, rGO–CuO18, rGO–CuO116 and rGO–CuO124 was found to be 310, 362, 474 and 498 μmol g^{-1} cat

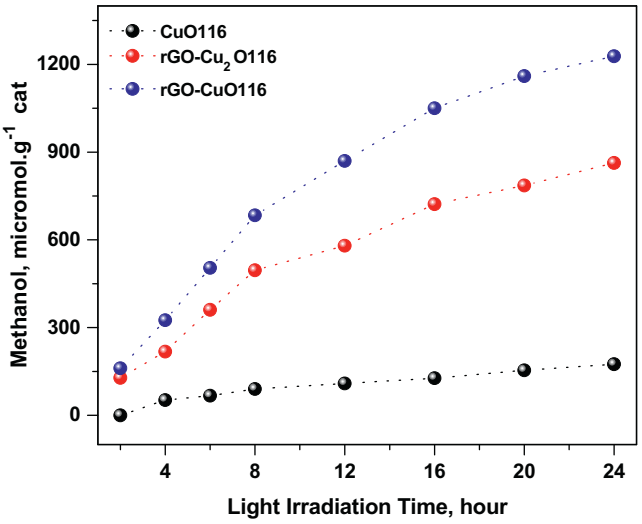

Fig. 9. Methanol yield by photocatalysis of CO_2 as a function of light irradiation time using CuO116, rGO–Cu_2O116 and rGO–CuO116 nanocomposites as photocatalysts.

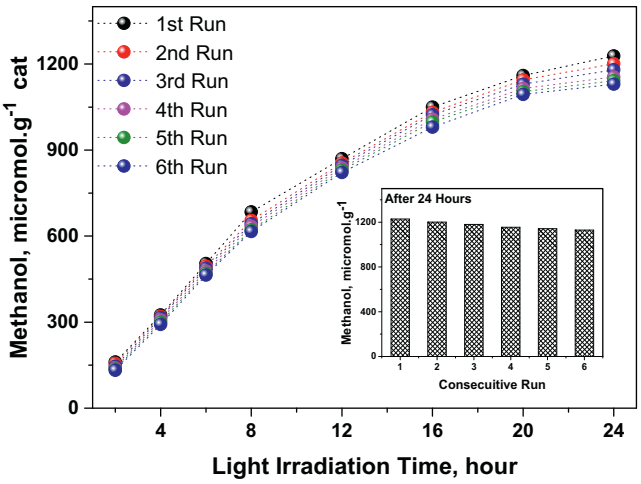

Fig. 10. Recycling of rGO–CuO116 photocatalyst for the methanol yield by photocatalytic reduction of CO_2 as a function of light irradiation time. Inset of figure shows methanol yield after 24 h of photocatalytic reaction for six consecutive runs.

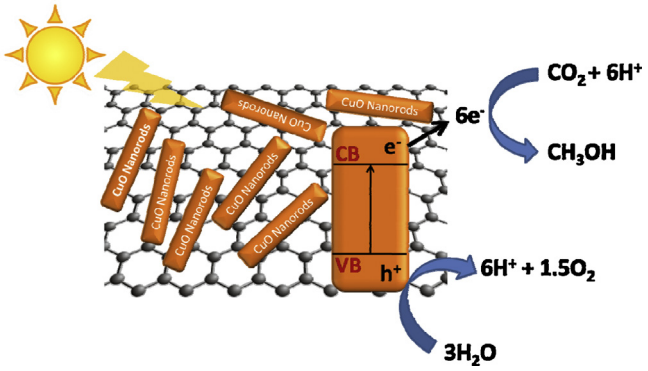

Fig. 11. Schematic illustration on plausible mechanism of photocatalytic conversion of CO_2 into the methanol using rGO–CuO nanocomposites under the visible light irradiation.

respectively, while the yield of oxygen was found to be 1064, 1270, 1582 and 1654 μmol g^{-1} cat respectively. The presence of oxygen in gaseous reaction products suggested that water splitting was the route of holes scavenging and providing protons and electrons required to complete the catalytic cycle. This fact was further confirmed by comparing the amount of evolved oxygen with the methanol. In all photocatalytic reactions, yield of oxygen was nearly 1.3 times than that of methanol and was in good agreement with the stoichiometry of reaction as shown in the proposed mechanism of CO_2 reduction (Fig. 11).

The effect of chemical grafting of CuO nanorods on rGO skeleton and oxidation state of copper in the developed nanocomposites on their photocatalytic activity were examined under visible light irradiation using three different photocatalysts; bare CuO116, rGO–Cu_2O116 (Cu^{+1}) and rGO–CuO116 (Cu^{+2}). As depicted in Fig. 9, these three catalysts showed photocatalytic activity and yielded methanol by photoreduction of CO_2. However, significant differences were observed in their activity. Bare CuO116 exhibited low activity because of fast recombination process and yielded methanol only 175 μmol g^{-1} cat after 24 h of visible light irradiation. The rGO–Cu_2O116 showed comparatively much better photocatalytic performance and yielded five folds methanol (862 μmol g^{-1} cat), whereas rGO–CuO116 exhibited excellent photocatalytic activity and yielded seven fold methanol (1228 μmol g^{-1} cat) as compared to that of CuO116 nanorods. Recently, it was revealed that rGO coating significantly increases the activity of Cu_2O for CO_2 photoreduction to CO; a nearly six times higher activity than the optimized Cu_2O [52]. It was attributed to retarded electron–hole recombination, efficient charge transfer and protective function of rGO. Herein, CuO (Cu^{+2}) nanorods grafted on rGO showed better photocatalytic activities than that of rGO–Cu_2O (Cu^{+1}) nanocomposite.

Stability and recyclability of the rGO–CuO116 catalyst was examined for photocatalytic conversion of CO_2 into methanol under visible light irradiation. The recovered rGO–CuO116 catalyst was reused for the five subsequent runs (Fig. 10). In all experiments, a yield of methanol remained almost the same. After, six cycles of photocatalytic reaction, the recovered rGO–CuO116 catalyst was examined by HRTEM and FTIR (Fig. S5 and S6, ESI) to probe the structural and chemical stability. No significant differences were observed in morphological and chemical features of pristine and recovered rGO–CuO116 catalyst, indicating that rGO–CuO116 catalyst is structurally and chemically stable under the photocatalytic reactions.

CuO nanomaterials absorb visible light of solar spectrum very efficiently and generate electron–hole pairs. However, owing to the narrow band gap, these electron–hole pairs recombine very fast, before they could be available for photocatalytic reaction. Therefore, bare CuO116 showed very low photocatalytic conversion (Fig. 9). The CuO116 nanorods grafted on the rGO skeleton revealed remarkable enhancement in their photocatalytic activity, which is most likely due to the nearly equal position of conduction band of CuO (~4.1 eV) and LUMO of graphene (~4.4 eV) [53,54]. Thus, the photo-generated electron in the conduction band of CuO can easily transfer to the rGO nanosheets, which inhibits the recombination of electron–hole pairs and facilitate the electron transport to the catalytic sites for reduction of CO_2. The rGO with large surface area and various defective sites are prone to absorb CO_2. The photo-generated electron on CuO nanorods are transmitted to the catalytic sites of rGO and then reduced the absorbed CO_2 into the methanol. Eventually, photo-generated holes oxidized the water molecules to give protons (H^+) [55]. The one mole of CO_2 and six moles of H^+ were reduced by interacting with six moles of photo-generated electrons as shown in Fig. 11. Consequently, one mole of methanol and 1.5 moles of oxygen should be generated. This was further supported by mole ratio of photo-generated methanol and oxygen, *i.e.*, 1:1.3.

4. Conclusions

Copper oxide (CuO and Cu_2O) nanomaterials were covalently grafted on the rGO nanosheets and then used for the photocatalytic reduction of CO_2 to methanol under visible light irradiation. The breadth of CuO nanorods in rGO–CuO nanocomposites was found to play an important role in controlling the photocatalytic activities. The grafting of CuO nanorods on rGO significantly increased the photocatalytic efficiency and provided nearly seven folds methanol yield in comparison to that of bare CuO nanorods. Furthermore, rGO–CuO (Cu^{+2}) showed superior photocatalytic activity than rGO–Cu_2O (Cu^{+1}) under identical conditions. The improved photocatalytic activities of CuO in rGO–CuO nanocomposites were attributed to the slow recombination of charge carrier and efficient charge transfer of photogenerated electrons through the rGO skeleton. Furthermore, the use of readily available and low cost metal oxide catalyst offers great potential for the visible light-assisted conversion of CO_2 into valuable chemicals in a sustainable manner.

Acknowledgements

We kindly acknowledge Director, CSIR-IIP for his permission to publish these results. RG is thankful to CSIR, New Delhi for research fellowship. We acknowledge ASD and RTD of CSIR-IIP, Dehradun for providing support in analysis. The authors are grateful to CSIR-CMCRI Bhavnagar and Kyoto University, Japan for their support with the HRTEM and XPS analyses.

Appendix A. Supplementary data

Supplementary data associated with this article can be found, in the online version, at http://dx.doi.org/10.1016/j.apcatb.2015.08.012

References

[1] A.A. Lacis, G.A. Schmidt, D. Rind, R.A. Reudy, Atmospheric CO_2: principal control knob governing Earth's temperature, Science 330 (2010) 356–359.
[2] K. Li, X. An, K.H. Parka, M. Khraisheh, J. Tang, A critical review of CO_2 photoconversion: catalysts and reactors, Catal. Today 224 (2014) 3–12.
[3] H.C. Hsu, I. Shown, H.Y. Wei, Y.C. Chang, H.Y. Du, Y.G. Lin, C.A. Tseng, C.H. Wang, L.C. Chen, Y.C. Lin, K.H. Chen, Graphene oxide as a promising photocatalyst for CO_2 to methanol conversion, Nanoscale 5 (2013) 262–268.
[4] F. Sastre, A.V. Puga, L. Liu, A. Corma, H. Garcia, Complete photocatalytic reduction of CO_2 to methane by H_2 under solar light irradiation, J. Am. Chem. Soc. 136 (2014) 6798–6801.
[5] T. Inoue, A. Fujishima, S. Konishi, K. Honda, Photoelectrocatalytic reduction of carbon dioxide in aqueous suspensions of semiconductor powders, Nature 277 (1979) 637–638.
[6] M. Mikkelsen, M. Jorgensen, F.C. Krebs, The teraton challenge. A review of fixation and transformation of carbon dioxide, Energy Environ. Sci. 3 (2010) 43–81.
[7] C. Costentin, M. Robert, J.M. Saveant, Catalysis of the electrochemical reduction of carbon dioxide, Chem. Soc. Rev. 42 (2013) 2423–2436.
[8] A.T. Najafabadi, CO_2 chemical conversion to useful products: an engineering insight to the latest advances toward sustainability, Int. J. Energy Res. 37 (2013) 485–499.
[9] V.P. Indrakanti, J.D. Kubicki, H.H. Schobert, Photoinduced activation of CO_2 on Ti-based heterogeneous catalysts: current state, chemical physics-based insights and outlook, Energy Environ. Sci. 2 (2009) 745–758.
[10] S.N. Habisreutinger, L. Schmidt-Mende, J.K. Stolarczyk, Photocatalytic reduction of CO_2 on TiO_2 and other semiconductors, Angew. Chem. Int. Ed. 52 (2013) 7372–7408.
[11] S. Das, W.M.A.W. Daud, A review on advances in photocatalysts towards CO_2 conversion, RSC Adv. 4 (2014) 20856–20893.
[12] Slamet, H.W. Nasution, E. Purnama, S. Kosela, J. Gunlazuardi, Photocatalytic reduction of CO_2 on copper-doped titania catalysts prepared by improved impregnation method, Catal. Commun. 6 (2005) 313–319.
[13] I. Shown, H.C. Hsu, Y.C. Chang, C.H. Lin, P.K. Roy, A. Ganguly, C.H. Wang, J.K. Chang, C.I. Wu, L.C. Chen, K.H. Chen, Highly efficient visible light photocatalytic reduction of CO_2 to hydrocarbon fuels by Cu-nanoparticle decorated graphene oxide, Nano Lett. 14 (2014) 6097–6103.
[14] S. Kumar, O.P. Khatri, S. Cordier, R. Boukherroub, S.L. Jain, Graphene oxide supported molybdenum cluster: first heterogenized homogeneous catalyst for the synthesis of dimethylcarbonate from CO_2 and methanol, Chem. Eur. J. 21 (2015) 3488–3494.
[15] S. Navalon, A. Dhakshinamoorthy, M. Alvaro, H. Garcia, Photocatalytic CO_2 reduction using non-titanium metal oxides and sulfides, Chem. Sus. Chem. 6 (2013) 562–577.
[16] J. Yang, D. Wang, H. Han, Roles of cocatalysts in photocatalysis and photoelectrocatalysis, Acc. Chem. Res. 46 (2013) 1900–1909.
[17] S. Wang, W. Yao, J. Lin, Z. Ding, X. Wang, Cobalt imidazole metal-organic frameworks photosplit CO_2 under mild reaction conditions, Angew. Int. Ed. 53 (2014) 1034–1038.
[18] S. Wang, J. Lin, X. Wang, Semiconductor-redox catalysis promoted by meal-organic frameworks for CO_2 reduction, Phys. Chem. Chem. Phys. 16 (2014) 14646–14660.
[19] S. Wang, X. Wang, Photocatalytic CO_2 reduction by CdS promoted with a zeolitic imidazolate framework, Appl. Catal. B Environ. 162 (2015) 494–500.
[20] S. Wang, Z. Ding, X. Wang, A stable $ZnCo_2O_4$ cocatalyst for photocatalytic CO_2 reduction, Chem. Commun. 51 (2015) 1517–1519.
[21] S. Wang, Y. Hou, X. Wang, The development of a stable $MnCo_2O_4$ cocatalyst for photocatalytic CO_2 reduction with visible light, ACS Appl. Mater. Interf. 7 (2015) 4327–4335.
[22] B. Cojocaru, S. Neatu, V.I. Parvulescu, K. Dumbuya, H.P. Steinruck, J.M. Gottfried, C. Aprile, H. Garcia, J.C. Scaiano, Band gap effect on the photocatalytic activity of supramolecular structures obtained by entrapping photosensitizers in different inorganic supports, Phys. Chem. Chem. Phys. 11 (2009) 5569–5577.
[23] M.A. Henderson, A. Michael, A surface science perspective on TiO_2 photocatalysis, Surf. Sci. Rep. 66 (2011) 185–297.
[24] S.H. Szczepankiewicz, A.J. Colussi, M.R. Hoffmann, Infrared spectra of photoinduced species on hydroxylated titania surfaces, J. Phys. Chem. B 104 (2000) 9842–9850.
[25] P.V. Kamat, Manipulation of charge transfer across semiconductor interface. A criterion that cannot be ignored in photocatalyst design, J. Phys. Chem. Lett. 3 (2012) 663–672.
[26] H. Fujiwara, H. Hosokawa, K. Murakoshi, Y. Wada, S. Yanagida, T. Okada, H. Kobayashi, Effect of surface structures on photocatalytic CO_2 reduction using quantized CdS nanocrystallites, J. Phys. Chem. B 101 (1997) 8270–8278.
[27] S. Sato, T. Morikawa, S. Saeki, T. Kajino, T. Motohiro, Visible-light-induced selective CO_2 reduction utilizing a ruthenium complex electrocatalyst linked to a p-type nitrogen-doped Ta_2O_5 semiconductor, Angew. Chem. 122 (2010) 5227–5231.
[28] W. Wang, S. Wang, X. Ma, J. Gong, Recent advances in catalytic hydrogenation of carbon dioxide, Chem. Soc. Rev. 40 (2011) 3703–3727.
[29] F. Schwierz, Graphene transistors, Nat. Nanotechnol. 5 (2010) 487–496.
[30] M.J. Allen, V.C. Tung, R.B. Kaner, Honeycomb carbon: a review of graphene, Chem. Rev. 110 (2010) 132–145.
[31] J.S. Bunch, A.M.V.D. Zande, S.S. Verbridge, I.W. Frank, D.M. Tanenbaum, J.M. Parpia, H.G. Craighead, P.L. McEuen, Electromechanical resonators from graphene sheets, Science 315 (2007) 490–493.
[32] M.D. Stoller, S. Park, Y. Zhu, J. An, R.S. Ruoff, Graphene-based ultracapacitors, Nano Lett. 8 (2008) 3498–3502.
[33] S. Guo, S. Dong, E. Wang, Three-dimensional Pt-on-Pd bimetallic nanodendrites supported on graphene nanosheet: facile synthesis and used as an advanced nanoelectrocatalyst for methanol oxidation, ACS Nano 4 (2010) 547–555.
[34] S. Choudhary, H.P. Mungse, O.P. Khatri, Dispersion of alkylated graphene in organic solvents and its potential for lubrication applications, J. Mater. Chem. 12 (2012) 21032–21039.
[35] P.V. Kamat, Graphene-based nanoassemblies for energy conversion, J. Phys. Chem. Lett. 2 (2011) 242–251.
[36] T.F. Yeh, J.M. Syu, C. Cheng, T.H. Chang, H. Teng, Graphite oxide as a photocatalyst for hydrogen production from water, Adv. Funct. Mater. 20 (2010) 2255–2262.
[37] I.V. Lightcap, T.H. Kosel, P.V. Kamat, Anchoring semiconductor and metal nanoparticles on a two-dimensional catalyst mat. Storing and shuttling electrons with reduced graphene oxide, Nano Lett. 10 (2010) 577–583.
[38] H. Zhang, X. Lv, Y. Li, Y. Wang, J. Li, P25-graphene composite as a high performance photocatalyst, ACS Nano 4 (2010) 380–386.
[39] W.J. Foo, C. Zhang, G.W. Ho, Non-noble metal Cu-loaded TiO_2 for enhanced photocatalytic H_2 production, Nanoscale 5 (2013) 759–764.
[40] S. Neatu, J.A. Macia-Agullo, P. Concepción, H. Garcia, Gold–copper nanoalloys supported on TiO_2 as photocatalysts for CO_2 reduction by water, J. Am. Chem. Soc. 136 (2014) 15969–15976.
[41] J.P. Yasomanee, J. Bandara, Multi-electron storage of photoenergy using Cu_2O–TiO_2 thin film photocatalyst, Solar Energy Mater. Solar Cells 92 (2008) 348–352.
[42] J. Tian, H. Li, Z. Xing, L. Wang, Y. Luo, A.M. Asiri, A.O. Al-Youbi, X. Sun, One-pot green hydrothermal synthesis of CuO–Cu_2O–Cu nanorod-decorated reduced graphene oxide composites and their application in photocurrent generation, Catal. Sci. Technol. 2 (2012) 2227–2230.
[43] H.P. Mungse, O.P. Sharma, H. Sugimura, O.P. Khatri, Hydrothermal deoxygenation of graphene oxide in sub- and supercritical water, RSC Adv. 4 (2014) 22589–22595.
[44] H.P. Mungse, O.P. Khatri, Chemically functionalized reduced graphene oxide as a novel material for reduction of friction and wear, J. Phys. Chem. C 118 (2014) 14394–14402.

[45] Joint Committee on Powder Diffraction Standards, JCPDS International Center for Diffraction Data, Pennsylvania, 1991.
[46] Y. Zhang, H. Tang, X. Ji, C. Li, L. Chen, D. Zhang, X. Yang, H. Zhang, Synthesis of reduced graphene oxide/Cu nanoparticle composites and their tribological properties, RSC Adv. 3 (2013) 26086–26093.
[47] C. Chen, H. Xu, L. Xu, F. Zhang, J. Dong, H. Wang, One-pot synthesis of homogeneous core–shell Cu_2O films with nanoparticle-composed multishells and their photocatalytic properties, RSC Adv. 3 (2013) 25010–25018.
[48] (a) C.K. Wu, M. Yin, S. O'Brien, J.T. Koberstein, Quantitative analysis of copper oxide nanoparticle composition and structure by X-ray photoelectron spectroscopy, Chem. Mater. 18 (2006) 6054–6058;
(b) J. Ghijsen, L.H. Tjeng, J.V. Elp, H. Eskes, J. Westerink, G.A. Sawatzky, M.T. Czyzyk, Electronic structure of Cu_2O and CuO, Phys. Rev. B 38 (1988) 11322.
[49] Y. Matsuo, T. Miyabe, T. Fukutsuka, Y. Sugie, Preparation and characterization of alkylamine-intercalated graphite oxides, Carbon 47 (2007) 1005–1012.
[50] H.P. Mungse, R. Singh, H. Sugimura, N. Kumar, O.P. Khatri, Molecular pillar supported graphene oxide framework: conformational heterogeneity and tunable D-spacing, Phys. Chem. Chem. Phys. 17 (2015) 20822–20829, http://dx.doi.org/10.1039/C5CP02313K
[51] C. Huo, J. Quyang, H. Yang, CuO nanoparticles encapsulated inside Al-MCM-41 mesoporous materials via direct synthetic route, Sci. Rep. (2014) 1–9.
[52] X. An, K. Li, J. Tang, Cu_2O/reduced graphene oxide composites for the photocatalytic conversion of CO_2, ChemSusChem. 7 (2014) 1086–1093.
[53] N. Yang, J. Zhai, D. Wang, Y. Chen, L. Jiang, Two-dimensional graphene bridges enhanced photoinduced charge transport in dye-sensitized solar cells, ACS Nano 4 (2010) 887–894.
[54] D. Chauhan, V.R. Satsangi, S. Dass, R. Srivastav, Preparation and characterization of nanostructured CuO thin films for photoelectrochemical splitting of water, Bull. Mater. Sci. 29 (2006) 709–716.
[55] J. Yu, J. Low, W. Xiao, P. Zhou, M. Jaroniec, Enhanced photocatalytic CO_2-reduction activity of anatase TiO_2 by coexposed {0 0 1} and {1 0 1} facets, J. Am. Chem. Soc. 136 (2014) 8839–8842.